Kramers dichroism in *PT*-symmetric magnets

Oles Matsyshyn, Ying Xiong, and Justin C. W. Song*
Division of Physics and Applied Physics, School of Physical and Mathematical Sciences, Nanyang Technological University, Singapore 637371, Singapore

(Received 12 July 2024; revised 16 September 2025; accepted 1 June 2026; published 13 July 2026)

The quantum states in doubly degenerate Kramers pairs can act as an internal degree of freedom. Here, we uncover a *Kramers dichroism* in *PT*-symmetric magnets: interband transitions induced by circularly polarized light irradiation can selectively polarize Kramers partnered states allowing to control the Kramers degree of freedom. In contrast, Kramers pairs optically excited by linearly polarized light remain in a completely mixed state. Strikingly, we find a class of second-order nonlinear responses that directly track the polarization between Kramers partnered states. Such Kramers nonlinearities can be pronounced producing large second-order nonlinear layer polarization responses activated by Kramers degeneracy in layered antiferromagnets. Together with Kramers dichroism, these render optical responses a novel means for accessing the Kramers degree of freedom and diagnosing their quantum state.

DOI: 10.1103/225j-wnv6

I. INTRODUCTION

Spin and its transformation properties under time reversal (T) place strong constraints on electronic states. A case in point is Kramers degeneracies: in the presence of T symmetry, states with odd half-integer spin occur in orthogonal pairs with the same energy [1]. Interestingly, Kramers pairs can persist even in magnetic materials. When both T and inversion, P, symmetries are broken but their composite PT symmetry is preserved, Kramers degeneracies survive with each electronic Bloch state at least doubly degenerate [2,3]. Such Kramers pairs are PT protected [4]. As a result, quantum pseudospin polarization between the PT-partnered states can act as an internal Kramers degree of freedom. Nevertheless, in its ground state, PT symmetry ensures that each Kramers pair exists in a completely mixed state with zero coherence.

Here, we argue that the Kramers degree of freedom can be directly accessed and addressed by light. We find that when photoexcited by circularly polarized light, a Kramers pseudospin polarization of the PT-partnered Kramers pairs naturally develops, allowing chiral light to control the Kramers degree of freedom. In contrast, linearly polarized light only pumps the total population of the Kramers pair. We term chiral optical control of Kramers pairs "Kramers dichroism."

Critically, we identify a class of observables—PT-odd observables—that are sensitive to the internal Kramers degree of freedom. PT-even observables such as (the well-studied) charge current [5–12] possess the same expectation value for both states in each Kramers pair and are *blind* to the pseudospin polarization between eigenstates in the Kramers pair. In contrast, PT-odd observables [e.g., electric polarization, magnetization, or spin polarization (SP)] possess distinct values for states in each Kramers pair allowing to directly probe the Kramers degree of freedom. When combined with Kramers dichroism, we uncover a range of Kramers nonlinearities: second-order nonlinear responses that are sensitive to the Kramers degree of freedom; Kramers nonlinearities are chiral manifesting only for chiral light and switching sign for opposite chiralities. For absorptive events (i.e., resonant transitions), Kramers nonlinearities are the only second-order chiral responses for PT-odd observables. This enables to readily differentiate from other types of responses and renders Kramers nonlinearities a useful means of tracking Kramers dichroism.

Our work is situated in a current surge of interest in PT-symmetric magnetic materials and devices [3,4,13–16]. While often treated as a spectator degree of freedom, we find that quantum pseudospin polarization sustained between states in the Kramers pairs is essential and can be optically addressed; they lead to pronounced second-order nonlinearities that readily manifest in a range of PT-symmetric magnetic materials. For instance, we find that even-layered $MnBi_2Te_4$ (MBT) [4,13] antiferromagnets can realize pronounced Kramers nonlinearity such as a light-induced nonlinear layer polarization (LP) that can be switched by both helicity and underlying Néel order. This illustrates how Kramers nonlinearities are a powerful means of controlling the layer degree of freedom and probing the underlying antiferromagentic order in quantum materials.

II. KRAMERS DEGREE OF FREEDOM AND PAIR TRANSITIONS

We begin by analyzing a Bloch Hamiltonian $H_0(\mathbf{p})$ with Bloch eigenstates $|u_n(\mathbf{p})\rangle$ and energy $\epsilon_n(\mathbf{p})$. Here,

*Contact author: justinsong@ntu.edu.sg

$\mathbf{p}$ is the momentum. For materials with PT symmetry, $\mathbf{PT}H_0(\mathbf{p})(\mathbf{PT})^{-1} = H_0(\mathbf{p})$ ensures that electrons (odd spin-half particles) occur in doubly degenerate Kramers pairs: at every $\mathbf{p}$, there exist two orthogonal states $|u_n(\mathbf{p})\rangle$ and $|u_{\bar{n}}(\mathbf{p})\rangle$ with the same energy $\epsilon_n(\mathbf{p}) = \epsilon_{\bar{n}}(\mathbf{p})$.

This degeneracy produces an internal Kramers degree of freedom. To see this, consider the block density matrix within the Kramers subspace of $\{|u_n(\mathbf{p})\rangle, |u_{\bar{n}}(\mathbf{p})\rangle\}$ that describes its occupation:

$$\hat{\boldsymbol{\rho}}^{\{n,\bar{n}\}} = \sum_{ij\in\{n,\bar{n}\}} \rho^n_{ij} |u_i(\mathbf{p})\rangle\langle u_j(\mathbf{p})|, \qquad \rho^n_{ij} = \left[\rho^n_0 \mathbb{I} + \boldsymbol{\kappa}^n \cdot \boldsymbol{\sigma}^n\right]_{ij}, \tag{1}$$

$\boldsymbol{\sigma}^n = (\sigma_x, \sigma_y, \sigma_z)$ are Pauli matrices in the $n, \bar{n}$ Kramers subspace, $2\rho^n_0$ is the total occupation of Kramers states, and $\boldsymbol{\kappa}^n$ is a three-dimensional Kramers Bloch vector in the Kramers subspace. Since superpositions of Kramers pairs are equally good eigenstates, we find $H_0(\mathbf{p})[\hat{\boldsymbol{\rho}}]_{ij\in\{n,\bar{n}\}} = \epsilon_n(\mathbf{p})[\hat{\boldsymbol{\rho}}]_{ij\in\{n,\bar{n}\}}$. Importantly, the total energy in the Kramers subspace $\mathrm{Tr}(H_0(\mathbf{p})[\hat{\boldsymbol{\rho}}]_{ij\in\{n,\bar{n}\}}) = 2\rho^n_0\epsilon_n(\mathbf{p})$ is *blind* to $\boldsymbol{\kappa}^n$. As a result, $\boldsymbol{\kappa}^n$ describes a Kramers degree of freedom: deviations away from equal occupation of the Kramers pair that do not change its energy.

Notice that $|\boldsymbol{\kappa}^n|$ cannot be gauged away. Even as the Kramers states within the degenerate subspace can be unitarily rotated (e.g., via SU(2) gauge transformation), the Kramers block density matrix contains two gauge-invariant quantities: $\mathrm{Tr}[\hat{\rho}^n] = 2\rho^n_0$ and $\det[\hat{\rho}^n] = (\rho^n_0)^2 - |\boldsymbol{\kappa}^n|^2$. As a result, $|\boldsymbol{\kappa}^n|$ is also gauge invariant and captures the pseudospin polarization sustained between the Kramers pairs. Notice that finite $|\boldsymbol{\kappa}^n|$ drives Kramers pairs away from a completely mixed state. As such, $|\boldsymbol{\kappa}^n|$ encodes a type of "coherence" inside the Kramers pair. Nevertheless, in the ground electronic state of PT-symmetric materials, $\boldsymbol{\kappa}$ is zero for every Kramers pair ensured by its PT symmetry: the ground state is in a completely mixed state.

Nonzero $\boldsymbol{\kappa}^n$, as we now argue, can be readily induced in excited states by photoexcitation. To show this, we consider the stroboscopic (drive period average) pumping of the Kramers vector $\boldsymbol{\kappa}^n$. Under a periodic drive $\hat{V}(t) = e\mathbf{E}(t)\cdot\hat{\mathbf{r}}e^{\eta t}$ with an oscillating electric field $\mathbf{E} = (\mathcal{E}_+ e^{-i\omega t} + \mathcal{E}_- e^{i\omega t})/2$, we find that the rate of change of the Kramers block density matrix $\langle\partial_t\rho^n_{ij}\rangle_t = \int_0^T [\lim_{\eta\to 0}\partial_t\rho^n_{ij}]dt/T$ as

$$\left\langle\partial_t\rho^n_{ij}\right\rangle_t = \frac{\pi e^2}{2\hbar}\sum_{\nu=\pm1}\mathcal{E}^\alpha_{-\nu}\mathcal{E}^\beta_\nu \sum_{l\in\{l,\bar{l}\}} r^\alpha_{il}r^\beta_{lj}f_{li}\delta(\nu\hbar\omega - \epsilon_{li}), \tag{2}$$

where $f_{li}(\mathbf{p}) = f[\epsilon_l(\mathbf{p})] - f[\epsilon_i(\mathbf{p})]$ is the difference of Fermi functions, with $\epsilon_l(\mathbf{p})$ the energy of state with momentum $\mathbf{p}$ in band $l \in \{l, \bar{l}\}$. Here, the interband Berry connection is $r^\alpha_{il} = A^\alpha_{il} = \langle i, \mathbf{p}|i\partial^\alpha_p|l, \mathbf{p}\rangle$ and η is an adiabatic turn-on parameter.

Equation (2) describes Kramers pair transitions. Unlike systems with nondegenerate electronic bands, the interband transitions for Kramers degenerate systems inevitably involve four states: from valence band $\{|u_v(\mathbf{p})\rangle, |u_{\bar{v}}(\mathbf{p})\rangle\}$ subspace to conduction band $\{|u_c(\mathbf{p})\rangle, |u_{\bar{c}}(\mathbf{p})\rangle\}$ subspace, e.g., Fig. 1(a) and Eq. (2) taking $i, j \in \{c, \bar{c}\}$ and $l \in \{v, \bar{v}\}$. The optical transition process in Kramers degenerate bands described in Eq. (2) cannot in general be understood as a simple sum of transitions in two independent sets of nondegenerate bands. Instead, Kramers pair optical transitions are readily understood to occur from one degenerate (valence) subspace to another degenerate (conduction) subspace.

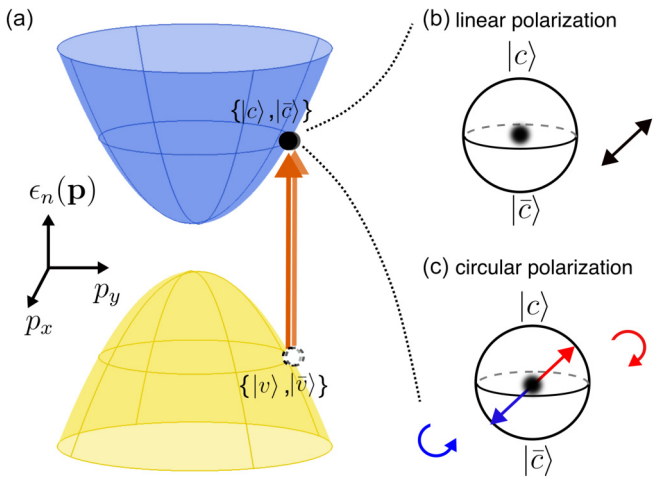

FIG. 1. Kramers Pair Optical Transitions. (a) Optical interband transitions in PT electronic bands involve Kramers *pairs* of degenerate states from $(v, \bar{v})$ to $(c, \bar{c})$. (b), (c) The quantum state after interband transition can be visualized in a Bloch sphere of the Kramers subspace, e.g., for $(c, \bar{c})$. (b) Linearly polarized light produces a completely mixed state in the Kramers subspace; black blurred dot denotes the trace of the density matrix in the Kramers subspace [Eq. (1)]. (c) In contrast, circularly polarized light produces a pseudospin polarization of the Kramers partnered states characterized by a Kramers Bloch vector $\boldsymbol{\kappa}$ (red, blue) [Eq. (1)]; $\boldsymbol{\kappa}$ can be switched by the helicity of light denoted by red and blue. We term the contrast between the quantum states induced by different light polarizations "Kramers Dichroism."

These Kramers pair transitions are essential in capturing a nonzero light-induced $\boldsymbol{\kappa}$. Comparing Eq. (2) with Eq. (1), we obtain the rate of change of Kramers Bloch vector magnitude as

$$|\langle\partial_t\boldsymbol{\kappa}^n\rangle_t| = \sqrt{\left|w^n_{n\bar{n}}\right|^2 + \frac{\left(w^n_{\bar{n}\bar{n}} - w^n_{nn}\right)^2}{4}}, \qquad w^n_{ij} \equiv \left\langle\partial_t\rho^n_{ij}\right\rangle_t, \tag{3}$$

demonstrating how the light-induced Kramers pair transitions induce pseudospin polarization in the Kramers doublet. Critically, $|\langle\partial_t\boldsymbol{\kappa}^n\rangle_t|$ in Eq. (3) is nonzero only for circularly polarized irradiation. In contrast, the achiral component of irradiation pumps $\langle\partial_t\rho^n_0\rangle_t$ the total population of the Kramers subspace (see Appendixes A and B). This means that $\partial_t\boldsymbol{\kappa}^n = 0$ for linearly polarized light, with $\boldsymbol{\rho}^{\{n,\bar{n}\}}$ in a completely mixed state. This shows that circularly polarized light irradiation allows to engineer the pseudospin polarization of Kramers pairs, optically controlling from maximally mixed (in the ground state) to partially coherent (in the excited state).

III. KRAMERS DICHROISM AND PT-ODD OBSERVABLES

How do we track the Kramers degree of freedom encoded in $\boldsymbol{\kappa}$? To proceed, we first note that PT symmetry places strong constraints on the matrix elements of PT-odd/even

observables $\mathbf{PT}\hat{O}^{(\pm)}(\mathbf{PT})^{-1} = \pm\hat{O}^{(\pm)}$ (see Appendix A):

$$O^{(\pm)}_{nn}(\mathbf{p}) = \pm O^{(\pm)}_{\bar{n}\bar{n}}(\mathbf{p}), \quad O^{(\pm)}_{n\bar{n}}(\mathbf{p}) = \mp O^{(\pm)}_{n\bar{n}}(\mathbf{p}), \tag{4}$$

where $(\pm)$ superscript indicate observables that are *PT* even (odd), respectively, and $O_{nm}(\mathbf{p}) = \langle n, \mathbf{p}|\hat{O}|m, \mathbf{p}\rangle$ is the matrix element for an observable $\hat{O}$. Using Eq. (4), we find that *PT*-even observables $\hat{O}^{(+)}$ are blind to $\boldsymbol{\kappa}^n$. For example, the charge current or the charge density $\hat{O}^{(+)} = \{e\hat{\mathbf{v}}, e\}$ is *PT* even. Evaluating their expectation value in the Kramers subspace yields $\mathrm{Tr}(\hat{O}^{(+)}\hat{\boldsymbol{\rho}}^{\{n,\bar{n}\}}) = 2\rho_0 O^{(+)}_{nn}(\mathbf{p})$.

In contrast, we find that *PT*-odd observables directly depend on $\boldsymbol{\kappa}^n$. Evaluating the *PT*-odd observable expectation value in the $\{n, \bar{n}\}$ Kramers subspace produces

$$\mathrm{Tr}[\hat{O}^{(-)}\hat{\boldsymbol{\rho}}^{\{n,\bar{n}\}}] = 2[\boldsymbol{O}^{(-)}_n] \cdot \boldsymbol{\kappa}^n, \quad \boldsymbol{O}^{(-)}_n = \tfrac{1}{2}\mathrm{Tr}[\boldsymbol{\sigma}_n \hat{O}^{(-)}], \tag{5}$$

which depends not only on the magnitude of $\boldsymbol{\kappa}^n$ but also the angle it subtends with $\boldsymbol{O}^{(-)}_n$. Notice that such expectations values are impossible without the Kramers subspace; without Kramers degeneracy, matrix elements of $\hat{O}^-$ vanish for *PT*-symmetric systems [see Eq. (4)].

As a result, optically pumped $\boldsymbol{\kappa}^n$ between the Kramers pairs in Eq. (3) can be directly probed by an injection nonlinearity for *PT*-odd observables. Using Eq. (2) and summing over initial and final states, we write the injection rate for $O^{(-)}$ observables as

$$\frac{dO^{(-)}}{dt} = \frac{\pi e^2}{2\hbar}\sum_{\nu=\pm1}\mathcal{E}^{\alpha}_{-\nu}\mathcal{E}^{\beta}_{\nu}\sum_{\mathbf{p},ijl} r^{\alpha}_{il} r^{\beta}_{lj} O^{(-)}_{ji} f_{li}\delta(\nu\hbar\omega - \epsilon_{li}), \tag{6}$$

which captures coherent Kramers pair transitions. Note that $l \in \{l, \bar{l}\}$, $\epsilon_i(\mathbf{p}) = \epsilon_j(\mathbf{p})$, and the $\mathbf{p}$ dependence of the quantities in Eq. (6) is implicit. Equation (6) vanishes for linearly polarized or achiral light but is turned on circularly polarized light directly mirroring the behavior of Eq. (3). We term the injection rate in Eq. (6) "Kramers injection (KI)" because not only does it depend on $\boldsymbol{\kappa}$, it also *vanishes* in *PT*-symmetric systems without Kramers degeneracy. This further underscores the critical role of the Kramers degree of freedom.

Interestingly, we find that Eq. (6) is controlled by $[\mathbf{E}_{-\omega} \times \mathbf{E}_{\omega}]$ (see Appendix B), changing signs for light with opposite circular polarization. Comparing with Eq. (5), this shows how changing the chirality of circularly polarized light flips the sign of light-induced $\boldsymbol{\kappa}$ and tracks a *Kramers dichroism*: opposite chiralities of light produce opposite $\boldsymbol{\kappa}$ vectors. Notice that *PT*-odd observables are zero in the ground state of *PT*-symmetric materials. This makes *PT*-odd observables (e.g., polarization and spin magnetization) ideal markers to track the internal Kramers degree of freedom and its hidden circular (Kramers) dichroism.

IV. KRAMERS NONLINEARITIES AND QUANTUM GEOMETRY

In the previous section, we focused on individual Kramers subspaces to illustrate the role of the Kramers dichroism. The responses associated with Kramers dichroism also naturally emerge from an analysis of the full density matrix where a natural separation into degenerate subspace responses and nondegenerate subspace response emerges; this analysis is discussed in full in Appendix C.

TABLE I. Table of $O^{(-)}$ second-order nonlinearities in *PT*-symmetric systems that contrast responses of Kramers degenerate (spinful, deg) versus nondegenerate (spinless, non-deg) *PT*-symmetric systems. Here, circular indicates difference between left hand and right hand. Note that while the Shift resonant (SR) and Shift Fermi sea responses do not require degeneracy to manifest, nevertheless, their formulas are affected by degeneracy (see Appendixes C and D).

PT	deg	nondeg	Light	Equation
Kramers injection	√	✗	circular	(8)
Kramers Fermi sea	√	✗	circular	(10)
Shift resonant	√	√	linear	(C8)
Shift Fermi sea	√	√	circular	(C9)

We now focus on how *PT*-odd observables can be connected to quantum geometry [8–12,17–23]. We do this by considering the set of Hamiltonians: $H_{\mathrm{eff}}(\lambda, \mathbf{p}) = H_0(\mathbf{p}) + \lambda\hat{O}^{(-)}$ parametrized by λ with Bloch eigenenergies $\varepsilon_n(\mathbf{p}, \lambda)$ and eigenstates $|\mathfrak{U}_n(\mathbf{p}, \lambda)\rangle$. Writing $\hat{O}^{(-)} = \partial_\lambda H_{\mathrm{eff}}$ produces an identity for $\tilde{O}^{(-)}_{nm}(\mathbf{p}, \lambda) = \langle\mathfrak{U}_n(\mathbf{p}, \lambda)|\, \hat{O}^{(-)}\, |\mathfrak{U}_m(\mathbf{p}, \lambda)\rangle$:

$$\tilde{O}^{(-)}_{nm}(\mathbf{p}, \lambda) = \partial_\lambda\varepsilon_n(\mathbf{p}, \lambda)\delta_{nm} + i\varepsilon_{nm}(\mathbf{p}, \lambda)\mathcal{A}^{\lambda}_{nm}(\mathbf{p}, \lambda), \tag{7}$$

where $\varepsilon_{nm}(\mathbf{p}, \lambda) = \varepsilon_n(\mathbf{p}, \lambda) - \varepsilon_m(\mathbf{p}, \lambda)$, and the λ-Berry connection is $\mathcal{A}^{\lambda}_{nm} = \langle\mathfrak{U}_n(\mathbf{p}, \lambda)|\, i\partial_\lambda\, |\mathfrak{U}_m(\mathbf{p}, \lambda)\rangle$. While $\lambda \neq 0$ breaks *PT* symmetry, thereby lifting degeneracy, $H_{\mathrm{eff}}(\lambda \to 0, \mathbf{p}) = H_0(\mathbf{p})$ restores its Kramers pairs. In what follows, we will take $\lambda \to 0$ in our final expressions so that $\tilde{O}^{(-)}_{nm}(\mathbf{p}, \lambda \to 0) = O^{(-)}_{nm}(\mathbf{p})$, with energies $\varepsilon_n(\mathbf{p}, \lambda \to 0) = \epsilon_n(\mathbf{p})$ and Bloch states $|\mathfrak{U}_m(\mathbf{p}, \lambda \to 0)\rangle = |u_m(\mathbf{p})\rangle$. Importantly, geometrical phases accrued in $\mathcal{A}^{\lambda}_{nm}$ persist even as $\lambda \to 0$, enabling to characterize $O^{(-)}$ nonlinearities with the quantum geometry of its states.

We proceed by systematically enumerating the second-order nonlinearites of *PT*-odd observables $O^{(-)}$. To do so, we employ the standard quantum Liouville treatment of nonlinear response [6,7,24] but generalized to *PT*-symmetric degenerate bands (see Appendix C for full details). Here, we report the main results for Kramers-induced second-order nonlinear susceptibilities of $\langle O^{(-)}\rangle = e^2\int d\omega\, E^{\alpha}_{-\omega}E^{\beta}_{\omega}\chi^{\alpha\beta}$.

We identify four second-order nonlinearities of *PT*-odd observables $\hat{O}^{(-)}$ (see Table I) associated with interband processes (see also below). The first is the Kramers injection nonlinearity [discussed above in Eq. (6)]. Using Eq. (7), the Kramers injection nonlinearity can be expressed in a compact geometrical form

$$\chi^{\alpha\beta}_{\mathrm{KI}} = \frac{\tau\pi}{4}\int_{\mathbf{p}}\sum_{nm}\delta(\hbar\omega - \varepsilon_{mn})f_{nm}i\left(v^{\alpha;\lambda}_{nm}\mathcal{A}^{\beta}_{mn} - v^{\alpha}_{nm}\mathcal{A}^{\beta;\lambda}_{mn}\right), \tag{8}$$

where v^{α}_{nm} is an interband velocity matrix element and $(;\lambda)$ denotes the generalized derivative

$$L^{\alpha;\lambda}_{mn} = \lim_{\lambda\to0}[D_\lambda, \hat{L}^{\alpha}]_{mn}, \quad D_\lambda = \partial_\lambda - i\mathcal{A}^{\lambda}\delta^{E} \tag{9}$$

of an operator $\hat{L}^{\alpha}$ (e.g., position or velocity). Note that $\lim_{\lambda\to0}\langle\mathfrak{U}_n(\mathbf{p}, \lambda)|\, \mathcal{A}^{\lambda}\delta^{E}\, |\mathfrak{U}_m(\mathbf{p}, \lambda)\rangle \equiv \mathcal{A}^{\lambda}_{nm}\delta_{\epsilon_n\epsilon_m}$ and $[\partial_\lambda, \hat{L}]_{mn} \equiv \partial_\lambda L_{mn}$. Importantly, the generalized derivative naturally sums across the degenerate Kramers states: it is U(2) covariant. As a result, when contracted with $v^{\alpha}_{nm}, \mathcal{A}^{\beta}_{nm}$,

it produces a gauge-invariant value. Just like other injection nonlinearities, the KI susceptibility in Eq. (8) is extrinsic and depends on an effective relaxation rate τ or pulse widths in an ultrafast measurement [22,23,25,26]. Notice that Kramers degeneracy modifies the constraint $\delta_{\epsilon_n\epsilon_m}$, yielding a shift response consistent with Kramers gauge invariance (see also below).

The second $O^{(-)}$ Kramers nonlinearity we find is a Kramers Fermi sea (KFS) susceptibility that is present even for a filled Fermi sea:

$$\chi^{\alpha\beta}_{\mathrm{KFS}} = \frac{\hbar}{2}\int_{\mathbf{p}}\sum_{nm} f_{nm} i\mathcal{P}\frac{v^{\alpha;\lambda}_{nm}\mathcal{A}^{\beta}_{mn} - v^{\alpha}_{nm}\mathcal{A}^{\beta;\lambda}_{mn}}{(\hbar\omega - \varepsilon_{mn})^2}. \tag{10}$$

Like the Kramers injection nonlinearity, it similarly vanishes in the absence of Kramers degeneracy for PT-symmetric systems. To see this, note that for nondegenerate PT-symmetric materials, the quantity $v^{\alpha;\lambda}_{nm}\mathcal{A}^{\beta}_{mn} - v^{\alpha}_{nm}\mathcal{A}^{\beta;\lambda}_{mn}$ when contracted with electric fields becomes proportional to $iA^{\alpha}_{nm}A^{\beta}_{mn}(O^{(-)}_{nn} - O^{(-)}_{mm})$; since $O^{(-)}_{nn}$ is zero in PT-symmetric nondegenerate electronic bands, $\chi^{\alpha\beta}_{\mathrm{KFS}}$ vanishes. In the same fashion as the KI nonlinearity, KFS only arises for circularly polarized light since $\chi^{\alpha\beta}_{\mathrm{KI,KFS}}(\omega) = -\chi^{\alpha\beta}_{\mathrm{KI,KFS}}(-\omega)$ in PT-symmetric materials: This makes $\chi^{\alpha\beta}_{\mathrm{KI,KFS}}$ pure imaginary and antisymmetric under $\alpha \leftrightarrow \beta$. In contrast to KI nonlinearity in Eq. (8), however, KFS does not require optical absorption and is nondissipative in nature, mirroring a dissipationless photocurrent nonlinearities that have attracted intense recent interest [6,24,27,28].

The last two $O^{(-)}$ nonlinearities we find in PT-symmetric materials are shift resonant (requires optical absorption) and shift Fermi sea nonlinearities (occurs even for frequencies under the gap) (see detailed discussion in Appendix C). Unlike KI and KFS, such shift resonant and shift Fermi sea $O^{(-)}$ nonlinearities persist even in nondegenerate PT-symmetric materials and do not directly track $\boldsymbol{\kappa}$. As shown in Table I, shift resonant $O^{(-)}$ in PT-symmetric systems manifests for linearly polarized light and can be readily distinguished from the KI and KFS responses via helicity-dependent irradiation. In contrast, shift Fermi sea $O^{(-)}$ is helicity sensitive. Even as such shiftlike nonlinearities do not need Kramers degeneracy to manifest, the presence of Kramers degeneracy nevertheless necessitates modifications to the expressions for shiftlike nonlinearities from its naïve nondegenerate form in much the same way as that of gyration photocurrents [9]. For a discussion of how the shift formulas are affected by degeneracy, see Appendixes C and D.

We note that the interband nonlinearities discussed above are present for both insulators and metals; in metals, however, additional nonlinearities associated with intraband processes become activated [29].

Finally, we note that while we have focused on presenting our results for $\hat{O}^{(-)}$ nonlinearities in the main text, our general density matrix formulation that treats both nondegenerate and degenerate cases found in Appendix C can be used for other observables as well. See Appendixes C and D for a full discussion including a discussion on its correspondence with the literature [9,12].

V. LIGHT-INDUCED NONLINEAR POLARIZATION IN $MnBi_2Te_4$

To illustrate Kramers dichroism, we examine even-layer $MnBi_2Te_4$: a PT-symmetric antiferromagnet (AFM). For simplicity, we focus on bilayer MBT; our qualitative conclusions are valid for other even layers. The electronic states of bilayer MBT can be captured by an effective eight-band Hamiltonian [30]: $H_0^{\mathrm{MBT}}(\mathbf{p}) = [h_1(\mathbf{p}),\ t\ ; t^{\dagger},\ h_2(\mathbf{p})]$. Here, $h_l(\mathbf{p})$ are layer Hamiltonians (layer index $l \in \{1,2\}$) that can be written as $h_l = h_N(\mathbf{p}) - x(-1)^l h_{\mathrm{AFM}}(\mathbf{p})$ [16,30]; t describes a $\mathbf{p}$-independent interlayer coupling that is PT symmetric (see Appendix E).

$h_N(\mathbf{p})$ describes a normal component that is the same in both layers: it is P and T invariant. It takes on the familiar Bernevig-Hughes-Zhang (BHZ) form [31]: $h_N(\mathbf{p}) = \epsilon_0(\mathbf{p})\tau_0\sigma_0 + m(\mathbf{p})\tau_z\sigma_z + v(p_x\tau_0\sigma_y + p_y\tau_0\sigma_x)$, with $\epsilon_0(\mathbf{p})$ and $m(\mathbf{p})$ the dispersive and massive contributions, and v is a velocity. Here, $\boldsymbol{\tau}$ and $\boldsymbol{\sigma}$ are Pauli matrices that describe orbital and spin degree of freedom in each layer. In contrast, $h_{\mathrm{AFM}} = \frac{1}{2}\mathrm{diag}[m_1, -m_2, m_2, -m_1]$ captures the Néel order; $x = \pm 1$ captures two distinct antiferromagnetic ground states with the same energy (see Fig. 2). Indeed, $-x(-1)^l h_{\mathrm{AFM}}$ breaks P and T symmetry but preserves PT symmetry. $H_0^{\mathrm{MBT}}(\mathbf{p})$ produces a band structure that is doubly degenerate at each $\mathbf{p}$ (Fig. 2, inset). Material parameters can be found in Appendix E.

To demonstrate Kramers dichroism in MBT, we now focus on circularly polarized light-induced $\hat{O}^{(-)}$ nonlinearities. These nonlinearities are PT odd. This is distinct from $\hat{O}^{(+)}$ observables such as the in-plane current [9] or indeed the antiferromagentic Néel order, both of which are PT even. We note that helicity-dependent optical control of antiferromagnetic order in MBT has recently been demonstrated experimentally [14].

A natural $\hat{O}^{(-)}$ observable in MBT is its layer polarization [29,32], $\hat{p}_z = \mathrm{diag}[\mathbb{I}_4, -\mathbb{I}_4]$. LP is odd under PT and possesses an expectation value that vanishes in the equilibrium state of PT-symmetric MBT. We numerically compute the $O^{(-)}$ nonlinearities described above of LP for H_0^{MBT} in Fig. 2(a) fixing the Fermi energy in the gap (see Appendix E for numerical details). We find that KI (blue)/KFS (purple) only manifest as a helicity-dependent response described by $\mathrm{Im}[\chi^{xy}_{\mathrm{LP}}(\omega)]$ and display a large and peaked response for frequencies close to transitions about the band extrema. In contrast, the shift Fermi sea nonlinear response for LP (shown in red) is almost two orders of magnitude smaller, demonstrating the dominant role that KI/KFS play in $\hat{O}^{(-)}$ nonlinearities allowing track the Kramers dichroism. Naturally, τ plays a critical role in the size of the nonlinearities. Here, we take on a phenomenological approach: in Appendix F, we plot other τ values from 1 fs to 1 ps that indicate that KI/KFS readily dominate over the shift Fermi sea response [19].

Another natural $\hat{O}^{(-)}$ observable in MBT is spin polarization: $\hat{s}_z = \frac{\hbar}{2} \times \mathrm{diag}[\sigma_z\tau_0, \sigma_z\tau_0]$. Similar to LP, Kramers SP nonlinearities are also helicity dependent [Fig. 2(b)]. However, unlike SP, $\mathrm{Im}[\chi^{xy}_{\mathrm{LP}}]$ exhibits a Néel order sensitivity, flipping sign when Néel order changes from $x = +1$ to $x = -1$ [Fig. 2(b)]. In contrast, $\mathrm{Im}[\chi^{xy}_{\mathrm{SP}}]$ retains its sign for both Néel orders; instead, its sign is locked to the helicity of the incident electro-magnetic field. This distinction between $\hat{O}^{(-)}$

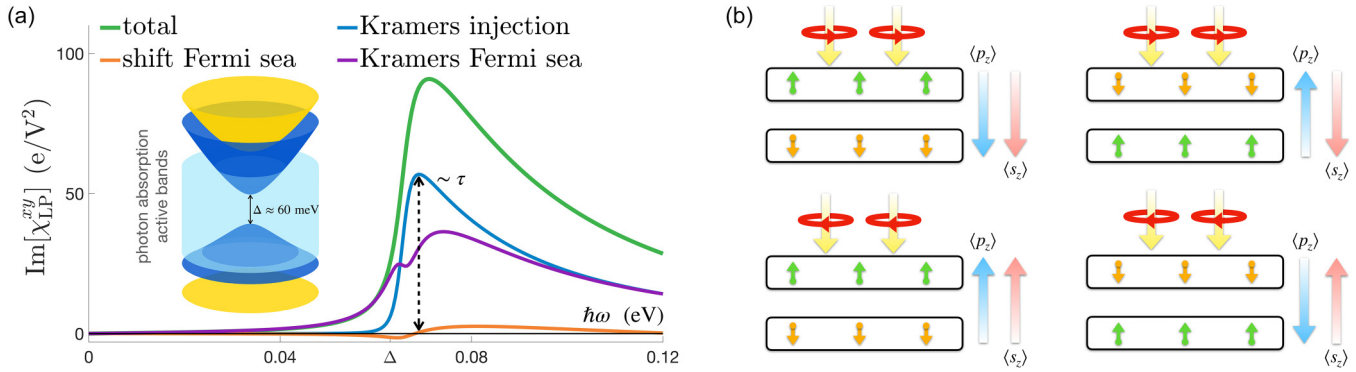

FIG. 2. Kramers activated second-order nonlinear responses in MBT. (a) Helicity-dependent nonlinear interlayer polarization susceptibility tensor of bilayer $MnBi_2Te_4$ ($\tau = 0.25$ ps [19], $\mu = 0.01$ eV; for the complete set of parameters, see Appendix E). Note that the KI response is the only circular response in the absorptive regime. While Fermi sea shift responses also display circular polarization sensitivity (orange), their effect is small as compared with KI (blue-cyan) and KFS (purple). Bilayer MBT band structure (left inset). (b) Schematic illustration of the interlayer polarization and spin responses for distinct circular (left-hand/right-hand) polarizations (red circular arrows) and Néel order parameters $x = \pm 1$, alternating according to the boxed arrow direction.

observables comports with the transformation properties of $\hat{p}_z$ and $\hat{s}_z$: P flips $\hat{p}_z$ and Néel order but preserves light helicity, while T flips $\hat{s}_z$, Néel order, and light helicity.

Kramers dichroism affords the ability to optically induce pseudospin polarization of Kramers partnered states in PT-symmetric magnets. While we have focused on the above bandgap noninteracting single-particle interband transitions, we anticipate pseudospin polarization between Kramers partners may persist also in the presence of interactions, e.g., in excitonic bound states that are formed from the superposition of particle-hole excitations between valence and conduction bands. Importantly, intra-Kramers-pair pseudospin polarization produces a class of second-order nonlinearities that allow to directly track optically induced superpositions. We find that they dominate the nonlinear response of layer polarization responses in MBT antiferromagnets. For instance, KI/KFS polarization susceptibilities $\mathrm{Im}[\chi^{xy}_{\mathrm{LP}}]$ of order $100\,\mathrm{e/V^2}$ readily dominate the interlayer polarization response of MBT; such KI/KFS nonlinearities are orders of magnitude larger than those recently found for twisted bilayer graphene [32]. Analogous to other optical responses, KI/KFS nonlinearities may also experience enhancements close to phase transitions [33] that can be readily controlled in two-dimensional magnetic platforms [34]. Kramers dichroism and nonlinearity together form a toolbox that can be used to prepare and map out superpositions of Kramers quantum states. We anticipate that this can open up the possibility of exploiting such coherences in a new type of quantum optoelectronics based off the Kramers degree of freedom.

ACKNOWLEDGMENTS

This research was supported by the Singapore Ministry of Education (MOE) Academic Research Fund Tier 2 Grant No. (MOE-T2EP50222-0011) Tier 3 Grant No. (MOE 2018-T3-1-002), and Tier 3 Grant No. (MOE-MOET32023-0003) "Quantum Geometric Advantage."

DATA AVAILABILITY

The data that support the findings of this article is publicly available at [36].

APPENDIX A: SYMMETRY PROPERTIES OF OPERATORS AND ZERO KRAMERS BLOCH VECTOR IN *PT*-SYMMETRIC GROUND STATE

In this Appendix, we will examine the constraints that PT symmetry places on states and matrix elements. We first note that for PT-partnered states $|u_n\rangle$ and $|u_{\bar{n}}\rangle$, we can write

$$PT|u_n\rangle = e^{i\phi_{n\bar{n}}}|u_{\bar{n}}\rangle, \quad PT|u_{\bar{n}}\rangle = e^{i\phi_{\bar{n}n}}|u_n\rangle, \tag{A1}$$

where ϕ angles are a general phase factor associated with the transformation. Since $(PT)^2 = -1$ (for fermionic electronic states), we have $(PT)^2|u_n\rangle = PTe^{i\phi_{n\bar{n}}}|u_{\bar{n}}\rangle = e^{-i\phi_{n\bar{n}}}PT|u_{\bar{n}}\rangle$; thus, $e^{i(\phi_{\bar{n}n}-\phi_{n\bar{n}})} = -1$.

Using the above, we can now examine the constraints that PT symmetry imposes on matrix elements of an operator $\hat{O}$. We will consider two sets of operators: PT even ($\xi = +1$) and PT odd ($\xi = -1$) so that $PT\hat{O}^{(\xi)}(PT)^{-1} = \xi\hat{O}^{(\xi)}$. We find that matrix elements of this operator satisfy

$$\begin{aligned}\langle u_m|\hat{O}|u_n\rangle &= e^{i\phi_{\bar{m}m}}e^{-i\phi_{\bar{n}n}}\xi\langle PTu_{\bar{m}}|PT\hat{O}(PT)^{-1}|PTu_{\bar{n}}\rangle \\ &= e^{i(\phi_{\bar{m}m}-\phi_{\bar{n}n})}\xi\langle PTu_{\bar{m}}|PT\hat{O}|u_{\bar{n}}\rangle \\ &= e^{i(\phi_{\bar{m}m}-\phi_{\bar{n}n})}\xi\langle\hat{O}u_{\bar{n}}|u_{\bar{m}}\rangle \\ &= e^{i(\phi_{\bar{m}m}-\phi_{\bar{n}n})}\xi\langle u_{\bar{m}}|\hat{O}|u_{\bar{n}}\rangle^* \\ &= e^{i(\phi_{\bar{m}m}-\phi_{\bar{n}n})}\xi\langle u_{\bar{n}}|\hat{O}|u_{\bar{m}}\rangle.\end{aligned} \tag{A2}$$

Using Eq. (A2), we can directly examine matrix elements in the Kramers subspace $\{n, \bar{n}\}$. Substituting the diagonal case $m = n$ as well as off diagonals $m = \bar{n}$, we obtain Eq. (4), reproduced here for the convenience of the reader:

$$O^{(\pm)}_{nn}(\mathbf{p}) = \pm O^{(\pm)}_{\bar{n}\bar{n}}(\mathbf{p}), \quad O^{(\pm)}_{n\bar{n}}(\mathbf{p}) = \mp O^{(\pm)}_{n\bar{n}}(\mathbf{p}). \tag{A3}$$

Importantly, we find that off-diagonal matrix elements for *PT*-even operators $O^{(+)}_{n\bar{n}}$ vanish. Similarly, its on-diagonal matrix elements are equal.

This can be directly applied to the density matrix in a PT-symmetric ground state. Notice that in the *PT*-symmetric ground state, the density matrix $\mathbf{PT}\hat{\boldsymbol{\rho}}^{\{n,\bar{n}\}}[\mathbf{PT}]^{-1} = \hat{\boldsymbol{\rho}}^{\{n,\bar{n}\}}$ is *PT* even. Hence, its off-diagonal matrix elements must vanish. As a result, $\boldsymbol{\kappa}^n_{x,y}$ vanish. Similarly, its *PT*-even character means that its on-diagonal matrix elements in the Kramers subspace are equal. As a result, we conclude that $\boldsymbol{\kappa}^n_z = 0$ also vanishes in the *PT*-symmetric ground state. Notice $\boldsymbol{\kappa}$ can be nonvanishing in the excited state. Indeed, as discussed in the main text, Kramers dichroism allows finite $\boldsymbol{\kappa}$ to develop.

APPENDIX B: RATE OF CHANGE OF KRAMERS BLOCK DENSITY MATRIX

The density matrix in the Kramers subspace can be directly obtained using a standard quantum Liouville approach (see discussion below). Focusing on the Kramers subspace $\{n, \bar{n}\}$ (i.e., $\epsilon_m(\mathbf{p}) = \epsilon_n(\mathbf{p})$), we find

$$\rho^{(2)}_{nm\in\{n,\bar{n}\}}(t) = \iint_{\omega_1,\omega_2} e^{-i(\omega_1+\omega_2)t+2\eta t/\hbar}\frac{e^2E^\alpha(\omega_2)E^\beta(\omega_1)}{\hbar(\omega_1+\omega_2)+2i\eta} \times \sum_c\left[\frac{r^\beta_{nc}r^\alpha_{cm}f_{nc}}{\hbar\omega_2-\epsilon_{cn}+i\eta} - \frac{r^\alpha_{nc}r^\beta_{cm}f_{cn}}{\hbar\omega_2-\epsilon_{nc}+i\eta}\right], \tag{B1}$$

where $\int_\omega \equiv \int_{-\infty}^{\infty} d\omega/(2\pi)$. For monochromatic light $\mathbf{E}(\omega_i) = 2\pi\sum_{\nu=\pm1}\boldsymbol{\mathcal{E}}_\nu\delta(\nu\omega-\omega_i)/2$, with $\boldsymbol{\mathcal{E}}_- = (\boldsymbol{\mathcal{E}}_+)^*$, the Kramers block density matrix above has the following rate of change:

$$\partial_t\rho^{(2)}_{nm\in\{n,\bar{n}\}}(t) = \frac{-ie^2}{4\hbar}\sum_{\nu,\nu'=\pm1}\mathcal{E}^\alpha_\nu\mathcal{E}^\beta_{\nu'}e^{-i(\nu+\nu')\omega t+2\eta t/\hbar} \times \sum_c\left[\frac{r^\beta_{nc}r^\alpha_{cm}f_{nc}}{\hbar\nu\omega-\epsilon_{cn}+i\eta} - \frac{r^\alpha_{nc}r^\beta_{cm}f_{cn}}{\hbar\nu\omega-\epsilon_{nc}+i\eta}\right]. \tag{B2}$$

Focusing on the rectified component (e.g., $\nu+\nu'=0$), we find Eq. (2). We note that this Kramers block density matrix is 2×2. To facilitate comparison with Eq. (1), we decompose into a trace and Kramers Bloch vector components as

$$\langle\partial_t\boldsymbol{\kappa}^n\rangle_t\cdot\boldsymbol{\sigma} = \int_0^T\frac{dt}{T}[\partial_t\boldsymbol{\kappa}^n\cdot\boldsymbol{\sigma}] = \begin{pmatrix}\frac{w^n_{nn}-w^n_{\bar{n}\bar{n}}}{2} & w^n_{n\bar{n}}\\ w^n_{\bar{n}n} & \frac{w^n_{\bar{n}\bar{n}}-w^n_{nn}}{2}\end{pmatrix}, \tag{B3}$$

where $2\langle\partial_t\rho^n_0\rangle_t = w^n_{\bar{n}\bar{n}}+w^n_{nn}$ and $w^n_{ij}\equiv\langle\partial_t\rho^n_{ij}\rangle_t$ denote individual components of the *rate of change* of the Kramers block density matrix written out for the convenience of the reader:

$$w^n_{ij} = \frac{\pi e^2}{2\hbar}\sum_{\nu=\pm1}\mathcal{E}^\alpha_{-\nu}\mathcal{E}^\beta_\nu\sum_c r^\alpha_{ic}r^\beta_{cj}f_{ci}\delta[\epsilon_{ci}-\nu\hbar\omega] = \frac{\pi e^2}{2\hbar\omega^2}\sum_{\nu=\pm1}\mathcal{E}^\alpha_{-\nu}\mathcal{E}^\beta_\nu\sum_c v^\alpha_{ic}v^\beta_{cj}f_{ci}\delta[\epsilon_{ci}-\nu\hbar\omega], \tag{B4}$$

where after relabeling dummy index ($\alpha\leftrightarrow\beta$) we have also used the identity $\mathbf{v} = (i/\hbar)[\mathbf{r}, H]$, where $\mathbf{v} = \hbar^{-1}\partial_{\mathbf{p}}\hat{H}(\mathbf{p})$, and for $\epsilon_i(\mathbf{p})\neq\epsilon_c(\mathbf{p})$, we have $\hbar v^\alpha_{ic} = i\epsilon_{ic}r^\alpha_{ic}$.

Applying Eq. (A2), we find that nonzero $\boldsymbol{\kappa}^n$ can be accessed only via the circularly polarized light irradiation. For the convenience of the reader, we show this explicitly. First, we apply Eq. (A2) onto

$$\begin{aligned}&\sum_{\nu=\pm1}\mathcal{E}^\alpha_{-\nu}\mathcal{E}^\beta_\nu\sum_c v^\alpha_{ic}v^\beta_{cj}f_{ci}\delta[\epsilon_{ci}-\nu\hbar\omega]\\ &= \sum_{\nu=\pm1}\mathcal{E}^\alpha_{-\nu}\mathcal{E}^\beta_\nu\sum_c e^{i(\phi_{\bar{i}i}-\phi_{\bar{j}j})}v^\alpha_{\bar{c}\bar{i}}v^\beta_{\bar{j}\bar{c}}f_{ci}\delta[\epsilon_{ci}-\nu\hbar\omega]\\ &= \sum_{\nu=\pm1}\left(\mathcal{E}^\alpha_{-\nu}\mathcal{E}^\beta_\nu\right)^*\sum_c e^{i(\phi_{\bar{i}i}-\phi_{\bar{j}j})}v^\alpha_{\bar{j}c}v^\beta_{c\bar{i}}f_{ci}\delta[\epsilon_{ci}-\nu\hbar\omega],\end{aligned} \tag{B5}$$

where for the last line of Eq. (B5) we used dummy relabeling ($\alpha\leftrightarrow\beta$). Notice that relabeling ($\bar{c}\to c$) does not affect energies.

We first examine the off-diagonal elements of the Kramers block density matrix $j=\bar{i}$ in Eq. (B4). Applying Eq. (B5) (note that $e^{i(\phi_{\bar{i}i}-\phi_{\bar{i}\bar{i}})} = -1$), we find

$$\begin{aligned}w^n_{i\bar{i}} &= \frac{\pi e^2}{2\hbar\omega^2}\sum_{\nu=\pm1}\mathcal{E}^\alpha_{-\nu}\mathcal{E}^\beta_\nu\sum_c v^\alpha_{ic}v^\beta_{c\bar{i}}f_{ci}\delta[\epsilon_{ci}-\nu\hbar\omega]\\ &= \frac{\pi e^2}{4\hbar\omega^2}\sum_{\nu=\pm1}\mathcal{E}^\alpha_{-\nu}\mathcal{E}^\beta_\nu\sum_c v^\alpha_{ic}v^\beta_{c\bar{i}}f_{ci}\delta[\epsilon_{ci}-\nu\hbar\omega]\\ &\quad-\frac{\pi e^2}{4\hbar\omega^2}\sum_{\nu=\pm1}\left(\mathcal{E}^\alpha_{-\nu}\mathcal{E}^\beta_\nu\right)^*\sum_c v^\alpha_{ic}v^\beta_{c\bar{i}}f_{ci}\delta[\epsilon_{ci}-\nu\hbar\omega]\\ &= \frac{i\pi e^2}{2\hbar\omega^2}\sum_{\nu=\pm1}\mathrm{Im}\left[\mathcal{E}^\alpha_{-\nu}\mathcal{E}^\beta_\nu\right]\sum_c v^\alpha_{ic}v^\beta_{c\bar{i}}f_{ci}\delta[\epsilon_{ci}-\nu\hbar\omega].\end{aligned} \tag{B6}$$

We can apply the same treatment to κ_z component:

$$\begin{aligned}w^n_{ii}-w^n_{\bar{i}\bar{i}} &= \frac{\pi e^2}{2\hbar\omega^2}\sum_{\nu=\pm1}\mathcal{E}^\alpha_{-\nu}\mathcal{E}^\beta_\nu\sum_c v^\alpha_{ic}v^\beta_{ci}f_{ci}\delta[\epsilon_{ci}-\nu\hbar\omega]\\ &\quad-\frac{\pi e^2}{2\hbar\omega^2}\sum_{\nu=\pm1}\mathcal{E}^\alpha_{-\nu}\mathcal{E}^\beta_\nu\sum_c v^\alpha_{ic}v^\beta_{c\bar{i}}f_{ci}\delta[\epsilon_{ci}-\nu\hbar\omega]\\ &= \frac{\pi e^2}{2\hbar\omega^2}\sum_{\nu=\pm1}\mathcal{E}^\alpha_{-\nu}\mathcal{E}^\beta_\nu\sum_c v^\alpha_{ic}v^\beta_{ci}f_{ci}\delta[\epsilon_{ci}-\nu\hbar\omega]\\ &\quad-\frac{\pi e^2}{2\hbar\omega^2}\sum_{\nu=\pm1}\left(\mathcal{E}^\alpha_{-\nu}\mathcal{E}^\beta_\nu\right)^*\sum_c v^\alpha_{ic}v^\beta_{ci}f_{ci}\delta[\epsilon_{ci}-\nu\hbar\omega]\\ &= \frac{i\pi e^2}{\hbar\omega^2}\sum_{\nu=\pm1}\mathrm{Im}\left[\mathcal{E}^\alpha_{-\nu}\mathcal{E}^\beta_\nu\right]\sum_c v^\alpha_{ic}v^\beta_{ci}f_{ci}\delta[\epsilon_{ci}-\nu\hbar\omega],\end{aligned} \tag{B7}$$

where in the second line we also employed Eq. (B5). From this calculation, we conclude that circularly polarized light controls Kramers degree of freedom in *PT* materials [see Eq. (B3)]. Importantly, as discussed in the main text, Eqs. (B7) and (B6) together with Eq. (B3) demonstrate that the direction

of the Kramers vector is reversed under switching the circular light polarization.

In contrast, for rate of change of the trace of the Kramers block density matrix, we find

$$w^n_{ii} + w^n_{\bar{i}\bar{i}} = \frac{\pi e^2}{\hbar\omega^2} \sum_{\nu=\pm1} \mathrm{Re}\big[\mathcal{E}^\alpha_{-\nu}\mathcal{E}^\beta_\nu\big] \sum_c v^\alpha_{ic} v^\beta_{ci} f_{ci}\delta[\epsilon_{ci} - \nu\hbar\omega], \tag{B8}$$

which is light helicity blind.

APPENDIX C: SYSTEMATIC QUANTUM LIOUVILLE APPROACH FOR NONLINEAR RESPONSE

In order to systematically derive the optical response of an electronic insulator (being careful to include the effects of Kramers degeneracy), we perturbatively solve the Liouville equation $i\hbar d_t\hat{\rho}(\mathbf{k},t) = [\hat{H}_0(\mathbf{k}) + \hat{V}(\mathbf{k},t), \hat{\rho}(\mathbf{k},t)]$, assuming that in equilibrium Bloch states are thermally populated $\langle n(\mathbf{k})|\,\hat{\rho}_{\rm eq}(\mathbf{k})\,|m(\mathbf{k})\rangle = f_{\rm FD}[\epsilon_n(\mathbf{k})]\delta_{nm}$. Here, $\hat{\rho}(\mathbf{k},t)$ is the density matrix. At second order, the correction to the rectified density matrix in the frequency domain is

$$\begin{aligned}\hat{\rho}^{(2)}_{mn} = e^2 \int_\omega E^\alpha_{-\omega}E^\beta_\omega e^{2\eta t/\hbar}\Bigg[&\frac{1}{\epsilon_{nm}+2i\eta} i\partial^\alpha_k \frac{A^\beta_{mn}f_{nm}}{\hbar\omega-\epsilon_{mn}+i\eta} \\ &+ \frac{1}{\epsilon_{nm}+2i\eta}\sum_c\Bigg\{\frac{A^\alpha_{mc}A^\beta_{cn}f_{nc}}{\hbar\omega-\epsilon_{cn}+i\eta} \\ &- \frac{A^\beta_{mc}A^\alpha_{cn}f_{cm}}{\hbar\omega-\epsilon_{mc}+i\eta}\Bigg\}\Bigg].\end{aligned} \tag{C1}$$

The nonlinear rectified response of any observable O represented by an operator $\hat{O}$ is given by $\langle O\rangle = \int_{\mathbf{p}}\sum_{nm} O_{nm}\rho_{mn}$. We write such explicitly by contracting Eq. (C1) with O_{nm} to find

$$\begin{aligned}O^{(2)}_{\rm inter} = e^2\int_{\mathbf{p}}\int_\omega E^\alpha_{-\omega}E^\beta_\omega e^{2\eta t/\hbar}\sum_{nm}\Bigg[&\frac{O_{nm}}{\epsilon_{nm}+2i\eta} i\partial^\alpha_k \\ &\times \frac{A^\beta_{mn}f_{nm}}{\hbar\omega+\epsilon_{nm}+i\eta} + \frac{A^\beta_{mn}f_{nm}}{\hbar\omega+\epsilon_{nm}+i\eta} \\ &\times \sum_c\Bigg\{\frac{O_{nc}A^\alpha_{cm}}{\epsilon_{nc}+2i\eta} - \frac{A^\alpha_{nc}O_{cm}}{\epsilon_{cm}+2i\eta}\Bigg\}\Bigg].\end{aligned} \tag{C2}$$

We note that the nonlinear susceptibility tensor $\chi^{\alpha\beta}(\omega)$ in $\int d\omega\, E^\alpha_{-\omega}E^\beta_\omega\chi^{\alpha\beta}$ has a "gauge" freedom. This is because when $\chi^{\alpha\beta}(\omega)$ contracted with a pair of electric fields, the physical response is symmetric under $\alpha\leftrightarrow\beta$, $\omega\leftrightarrow-\omega$:

$$\begin{aligned}\sum_{\alpha\beta}\int_\omega E^\alpha_{-\omega}E^\beta_\omega\chi^{\alpha\beta}(\omega) = \frac{1}{2}\sum_{\alpha\beta}\int_\omega E^\alpha_{-\omega}E^\beta_\omega(&\chi^{\alpha\beta}(\omega) \\ &+ \chi^{\beta\alpha}(-\omega)).\end{aligned} \tag{C3}$$

In what follows, as well as in the main text, we write the susceptibility tensors in a *symmetrized* form.

Interestingly, altermagnets [35] provide another interesting platform for physics involving degenerate pairs, as *XT*-protected degeneracies could in principle enable analogous pseudospin polarization-induced nonlinear responses. However, their quantitative contribution depends on the phase-space measure of the degenerate manifold. When degeneracies occur only at isolated points or lines, their contribution is expected to be small.

1. Kramers nonlinearities

The different terms of Eq. (C2) represent distinct nonlinearities. We first focus on the second term in the square brackets of Eq. (C2). Importantly, the first term in curly brackets when $\epsilon_c = \epsilon_n$ and the second term for $\epsilon_c = \epsilon_m$ are proportional to $1/\eta$. For small η, these terms are large. As we will now see, these terms form Kramers nonlinearities. Focusing on these nonlinear response terms in Eq. (C2) and writing them in a *symmetrized* form, we obtain

$$\begin{aligned}O^{(2)}_{\rm Kramers} = \frac{e^2}{2}\int_{\mathbf{p}}\int_\omega E^\alpha_{-\omega}E^\beta_\omega e^{2\eta t/\hbar}\sum_{nm}\frac{A^\beta_{mn}f_{mn}}{(\hbar\omega+\epsilon_{nm})^2+\eta^2} \\ \times\Bigg\{\sum_{c,\epsilon_c=\epsilon_n} O_{nc}A^\alpha_{cm} - \sum_{c,\epsilon_c=\epsilon_m} A^\alpha_{nc}O_{cm}\Bigg\}.\end{aligned} \tag{C4}$$

Next, we observe the following identity:

$$\begin{aligned}\lim_{\eta\to0}\frac{1}{(\hbar\omega+\epsilon_{nm})^2+\eta^2} &= \lim_{\eta\to0}\frac{\eta^2}{((\hbar\omega+\epsilon_{nm})^2+\eta^2)^2} \\ &\quad+ \lim_{\eta\to0}\frac{(\omega+\epsilon_{nm})^2}{((\hbar\omega+\epsilon_{nm})^2+\eta^2)^2} \\ &= \frac{\pi}{2\eta}\delta(\hbar\omega+\epsilon_{nm}) + \mathcal{P}\frac{1}{(\hbar\omega+\epsilon_{nm})^2}.\end{aligned} \tag{C5}$$

Applying the above identity to Eq. (C4), we obtain the KI nonlinearity as

$$\begin{aligned}O^{(2)}_{\rm KI} = \frac{\pi e^2}{4\eta}e^{2\eta t/\hbar}\int_\omega E^\alpha_{-\omega}E^\beta_\omega\int_{\mathbf{p}}\sum_{nm}\delta(\hbar\omega-\epsilon_{mn}) \\ \times f_{mn}A^\beta_{mn}\Bigg\{\sum_{c,\epsilon_c=\epsilon_n} O_{nc}A^\alpha_{cm} - \sum_{c,\epsilon_c=\epsilon_m} A^\alpha_{nc}O_{cm}\Bigg\},\end{aligned} \tag{C6}$$

and KFS nonlinearity as

$$\begin{aligned}O^{(2)}_{\rm KFS} = \frac{e^2}{2}\int_\omega E^\alpha_{-\omega}E^\beta_\omega e^{2\eta t/\hbar}\int_{\mathbf{p}}\sum_{nm}\mathcal{P}\frac{A^\beta_{mn}f_{mn}}{(\hbar\omega-\epsilon_{mn})^2} \\ \times\Bigg\{\sum_{c,\epsilon_c=\epsilon_n} O_{nc}A^\alpha_{cm} - \sum_{c,\epsilon_c=\epsilon_m} A^\alpha_{nc}O_{cm}\Bigg\}.\end{aligned} \tag{C7}$$

Note that taking a time derivative of the Kramers injection nonlinearity in Eq. (C6) in the limit of $\eta\to0$ yields Eq. (6). This corresponds to the resonant (absorptive) part of of Eq. (C4). As we will see below, by using the λ formulation, the quantum geometric content of Eq. (C6) can be revealed [see, e.g., Eq. (8)].

Equation (C7) corresponds to the Fermi sea component of Eq. (C4) and arises even in the absence of any absorption. By using the λ formulation, this KFS nonlinearity in Eq. (C7) produces Eq. (10). The above forms are numerically friendly, and was employed to produce Fig. 2.

2. Shift resonant and shift Fermi sea nonlinearities

Considering the rest of the terms in Eq. (C2), we find two sets of shift nonlinearities: a shift resonant and a shift Fermi sea contribution. After integrating by parts for ∂_k^α in Eq. (C2), we find an SR and SFS components as

$$\delta O^{(2)}_{\rm SR} = \pi e^2 \int_\omega E^\alpha_{-\omega} E^\beta_\omega \int_{\mathbf{p}} \sum_{nm} \delta(\hbar\omega - \epsilon_{mn}) A^\beta_{mn} f_{mn} \left[\partial^\alpha_{\mathbf{k}} \frac{O_{nm}}{\epsilon_{nm}} - i \left\{ \sum_{c,\epsilon_c \neq \epsilon_m} A^\alpha_{nc} \frac{O_{cm}}{\epsilon_{cn}} - \sum_{c,\epsilon_c \neq \epsilon_n} \frac{O_{nc}}{\epsilon_{nc}} A^\alpha_{cm} \right\} \right], \tag{C8}$$

$$\delta O^{(2)}_{\rm SFS} = e^2 \int_\omega E^\alpha_{-\omega} E^\beta_\omega \int_{\mathbf{p}} \sum_{nm} \mathcal{P} \frac{i A^\beta_{mn} f_{mn}}{\hbar\omega - \epsilon_{mn}} \left[\partial^\alpha_{\mathbf{k}} \frac{O_{nm}}{\epsilon_{nm}} - i \left\{ \sum_{c,\epsilon_c \neq \epsilon_m} A^\alpha_{nc} \frac{O_{cm}}{\epsilon_{cn}} - \sum_{c,\epsilon_c \neq \epsilon_n} \frac{O_{nc}}{\epsilon_{nc}} A^\alpha_{cm} \right\} \right], \tag{C9}$$

where we have used the identity $\lim_{\eta\to 0} 1/(x+i\eta) = \mathrm{P}(1/x) - i\pi\delta(x)$ to separate the contributions.

A numerically friendly form of the expression in the brackets is

$$\partial^\beta_{\mathbf{k}} \frac{O_{mn}}{\epsilon_{mn}} - i \left[\sum_{c,\epsilon_c \neq \epsilon_n} A^\beta_{mc} \frac{O_{cn}}{\epsilon_{cn}} - \sum_{c,\epsilon_c \neq \epsilon_m} \frac{O_{mc}}{\epsilon_{mc}} A^\beta_{cn} \right] = \frac{\langle m| \frac{\partial \hat{O}}{\partial k^\beta} |n\rangle}{\epsilon_{mn}} + \frac{1}{\epsilon^2_{mn}} \left[\sum_{c,\epsilon_c = \epsilon_n} v^\beta_{mc} O_{cn} - \sum_{c,\epsilon_c = \epsilon_m} v^\beta_{cn} O_{mc} \right] + \frac{1}{\epsilon_{mn}} \left[\sum_{c,\epsilon_c \neq \epsilon_m} \frac{O_{mc} v^\beta_{cn}}{\epsilon_{mc}} - \sum_{c,\epsilon_c \neq \epsilon_n} \frac{v^\beta_{mc} O_{cn}}{\epsilon_{cn}} \right]. \tag{C10}$$

3. Nonlinear responses for current

In the above, we showed a general formulation for treating second-order responses. In this Appendix, we demonstrate how our formulation naturally applies for the *PT*-even observables, in particular, photocurrent. Using $O = e\hat{\mathbf{v}}$ with $\hbar v^\gamma_{nm} = \delta_{nm}\partial^\gamma_{\mathbf{k}}\epsilon_n + i\epsilon_{nm}A^\alpha_{nm}$, we find that Eqs. (C6) and (C7) reduce to the standard resonant injection current [9,12]:

$$j^\gamma_{\rm injection} = \frac{\pi e^3}{4\eta} e^{2\eta t} \int_{\mathbf{p}} \int_\omega E^\alpha_{-\omega} E^\beta_\omega \sum_{nm} \delta(\hbar\omega - \epsilon_{mn}) \times A^\beta_{mn} A^\alpha_{nm} f_{mn} \left(v^\gamma_{nn} - v^\gamma_{mm} \right), \tag{C11}$$

and injection current principal part [9]:

$$j^\gamma_{\rm injection\ principal} = \frac{e^3}{2} \int_{\mathbf{p}} \int_\omega E^\alpha_{-\omega} E^\beta_\omega e^{2\eta t} \times \sum_{nm} \mathcal{P} \frac{A^\beta_{mn} A^\alpha_{nm} f_{mn}}{(\hbar\omega - \epsilon_{mn})^2} \left(v^\gamma_{nn} - v^\gamma_{mm} \right). \tag{C12}$$

The set of shift nonlinearities as shown in Eqs. (C8) and (C9) is also consistent with Refs. [9,12]. To see this for the shift photocurrent, we employ the identity

$$\partial^\beta_{\mathbf{k}} \frac{\hbar v^\gamma_{mn}}{\epsilon_{mn}} - i \left[\sum_{c,\epsilon_c \neq \epsilon_n} A^\beta_{mc} \frac{\hbar v^\gamma_{cn}}{\epsilon_{cn}} - \sum_{c,\epsilon_c \neq \epsilon_m} \frac{\hbar v^\gamma_{mc}}{\epsilon_{mc}} A^\beta_{cn} \right] = i\partial^\gamma_{\mathbf{k}} A^\beta_{mn} + \left(\sum_{c,\epsilon_c = \epsilon_m} A^\gamma_{mc} A^\beta_{cn} - \sum_{c,\epsilon_c = \epsilon_n} A^\beta_{mc} A^\gamma_{cn} \right), \tag{C13}$$

where we used $\partial^\gamma_{\mathbf{k}} A^\beta_{mn} - \partial^\beta_{\mathbf{k}} A^\gamma_{mn} = i\sum_c \{A^\gamma_{mc} A^\beta_{cn} - A^\beta_{mc} A^\gamma_{cn}\}$. Our formulation naturally takes care of degeneracies allowing to transparently produce the subtle U(2) gauge-invariant form of circular shift currents in *PT*-symmetric systems (see Ref. [9]). Notice that for nondegenerate systems, condition $\epsilon_n = \epsilon_m$ implies $n = m$; thus, we identify the shift vector as $i\partial^\gamma_{\mathbf{k}} A^\beta_{mn} + A^\beta_{mn}(A^\gamma_{mm} - A^\gamma_{nn}) = A^\beta_{mn} R^{\gamma;\beta}_{mn}$, where $R^{\gamma;\beta}_{mn} = i\partial^\gamma_{\mathbf{k}} \arg[A^\beta_{mn}] + A^\gamma_{mm} - A^\gamma_{nn}$. Once substituted in Eq. (C8), we find the resonant shift photocurrent as in Eq. (4) of Ref. [12]. Notice that for $O = e\hat{\mathbf{v}}$, Eq. (C9) produces an off-resonant principal part of the shift current; when combined with the injection current principal part, it produces a Fermi surface term consistent with Refs. [9,26].

APPENDIX D: KRAMERS QUANTUM GEOMETRY AND λ FORMULATION

In this Appendix, we massage the KI, KFS, and shiftlike nonlinearities to their compact geometrical form as shown in the main text. As in the main text, we examine the set of parametric Hamiltonians $H_{\rm eff}(\lambda, \mathbf{p}) = H_0(\mathbf{p}) + \lambda\hat{O}^{(-)}$, allowing us to write $\hat{O}^{(-)} = \partial H_{\rm eff}/\partial\lambda$, with the matrix elemets as in Eq. (7).

It is important to note that the λ term lifts the exact *PT* symmetry protected degeneracy of Kramers states, since $\hat{O}^{(-)}$ is *PT* odd. In order to explicitly track the states that in the limit of $\lambda \to 0$ become Kramers degenerate, it is useful to denote such states via $\varepsilon_n \approx \varepsilon_c$. Naturally, in the limit $\lambda \to 0$, the exact degeneracy of the equality is restored: $\approx \to =$. Using this notation, we write the Kramers nonlinearities as

$$\delta O^{(2)}_{\rm Kramers} = \frac{e^2}{2} \int_\omega E^\alpha_{-\omega} E^\beta_\omega \int_{\mathbf{p}} \sum_{nm} \left[\frac{\mathcal{A}^\beta_{mn} f_{mn}}{(\hbar\omega - \varepsilon_{mn})^2 + \eta^2} \times \left\{ \sum_{c,\varepsilon_c \approx \varepsilon_n} O_{nc} \mathcal{A}^\alpha_{cm} - \sum_{c,\varepsilon_c \approx \varepsilon_m} \mathcal{A}^\alpha_{nc} O_{cm} \right\} \right]. \tag{D1}$$

Employing the covariant derivative with respect to λ as

$$S^{\alpha;\lambda}_{mn} \equiv \partial^\lambda S^\alpha_{mn} - i \left[\sum_{c,\varepsilon_c \approx \varepsilon_m} \mathcal{A}^\lambda_{mc} S^\alpha_{cn} - \sum_{c,\varepsilon_c \approx \varepsilon_n} S^\alpha_{mc} \mathcal{A}^\lambda_{cn} \right], \tag{D2}$$

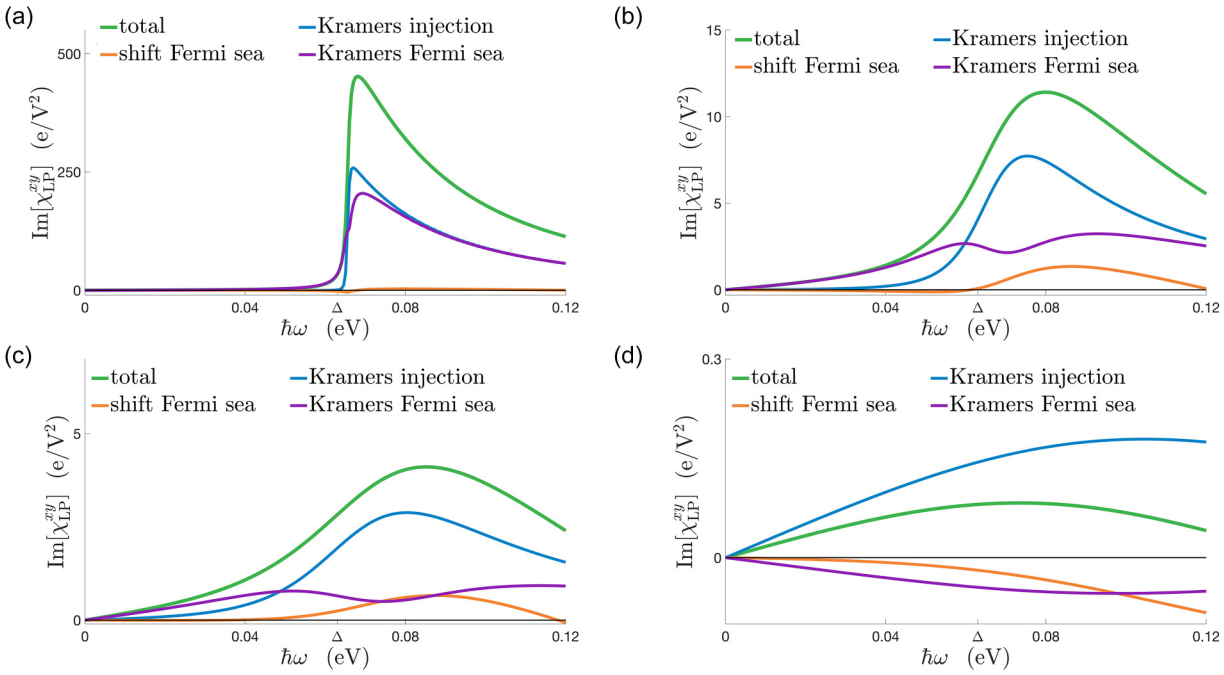

FIG. 3. Second-order nonlinear responses for *PT*-odd observables in MBT. Helicity-dependent nonlinear interlayer polarization susceptibility tensor of bilayer $MnBi_2Te_4$ for $\mu = 0.01$eV and (a) $\tau = 1$ ps, (b) $\tau = 50$ fs, (c) $\tau = 25$ fs, and (d) $\tau = 1$ fs; for the complete set of parameters, see Appendix E. Similar to the result displayed in Fig. 2(a), for the relaxation times shown, Kramers nonlinearities (KI and KFS) are larger than the shift Fermi sea nonlinearity. Notice that shift resonant contribution is helicity blind; as a result, $\frac{1}{2}\delta O^{(2)}_{\mathrm{SR}}(\mathrm{LH}) - \frac{1}{2}\delta O^{(2)}_{\mathrm{SR}}(\mathrm{RH})$ vanishes in a *PT*-symmetric material.

we find the following identity:

$$\hbar\nabla_\lambda v^\alpha_{nm} - i\epsilon_{nm}\nabla_\lambda A^\alpha_{nm} = i\sum_{c,\varepsilon_c\approx\varepsilon_n} O_{nc}\mathcal{A}^\alpha_{cm} - i\sum_{c,\varepsilon_c\approx\varepsilon_m}\mathcal{A}^\alpha_{nc}O_{cm}. \tag{D3}$$

In order to obtain the susceptibilities in the main text, we first note that the rectified responses of *PT*-odd observables to monochromatic electric fields of frequency Ω can be written generally as

$$\delta O^{(2)} = e^2\underbrace{(\mathcal{E}^\alpha\mathcal{E}^{*\beta} + \mathcal{E}^{*\alpha}\mathcal{E}^\beta)}_{\text{helicity blind}}\frac{1}{2}[\chi^{\alpha\beta}(\Omega) + \chi^{\alpha\beta}(-\Omega)] + e^2\underbrace{(i\mathcal{E}^\alpha\mathcal{E}^{*\beta} - i\mathcal{E}^{*\alpha}\mathcal{E}^\beta)}_{\text{helicity sensitive}}\frac{1}{2i}[\chi^{\alpha\beta}(\Omega) - \chi^{\alpha\beta}(-\Omega)]. \tag{D4}$$

After substitution of Eq. (D3) into Eq. (D1) and using Eq. (C5), we find the KI and KFS susceptibilities displayed in Eqs. (8) and (10), respectively. Notice that *PT* symmetry means that $\chi_{\mathrm{KI}}(\omega) = -\chi_{\mathrm{KI}}(-\omega)$ and $\chi_{\mathrm{KFS}}(\omega) = -\chi_{\mathrm{KFS}}(-\omega)$, which combined with Eq. (D4) implies that both are helicity dependent.

We now turn to the shift resonant and shift Fermi sea response. Using the fact that $\sum_{c,\varepsilon_c\neq\varepsilon_n} = \sum_c - \sum_{c,\varepsilon_c\approx\varepsilon_n}$, and the following identity for the Berry connections: $\partial^\alpha_k\mathcal{A}^\lambda_{nm} - i\sum_c[\mathcal{A}^\alpha_{nc}\mathcal{A}^\lambda_{cm} - A^\lambda_{nc}\mathcal{A}^\alpha_{cm}] = \partial^\lambda\mathcal{A}^\alpha_{nm}$, we can rewrite two shift nonlinear susceptibilities as

$$\chi^{\alpha\beta}_{\mathrm{SR}}(\omega) = \frac{\pi}{2}\int_{\mathbf{p}}\sum_{nm}\delta(\hbar\omega - \varepsilon_{mn})f_{mn}i\big(\mathcal{A}^{\alpha;\lambda}_{nm}\mathcal{A}^\beta_{mn} - \mathcal{A}^\alpha_{nm}\mathcal{A}^{\beta;\lambda}_{mn}\big), \tag{D5}$$

$$\chi^{\alpha\beta}_{\mathrm{SFS}}(\omega) = \frac{1}{2}\int_{\mathbf{p}}\sum_{nm}\big(\mathcal{A}^{\alpha;\lambda}_{nm}\mathcal{A}^\beta_{mn} + \mathcal{A}^\alpha_{nm}\mathcal{A}^{\beta;\lambda}_{mn}\big)\mathcal{P}\frac{f_{nm}}{\hbar\omega - \varepsilon_{mn}}. \tag{D6}$$

Much like Eq. (8), both shift resonant and shift Fermi sea nonlinearities in Eqs. (D5) and (D6) depend on a generalized covariant derivative that includes the Kramers pairs. Importantly, *PT* symmetry restricts shift resonant response to be helicity blind: $\chi_{\mathrm{SR}}(\omega) = \chi_{\mathrm{SR}}(-\omega)$, and thus, it identically vanishes in Figs. 2 and 3. In contrast, however, the shift Fermi sea is helicity sensitive, since for *PT*, we have $\chi_{\mathrm{SFS}}(\omega) = -\chi_{\mathrm{SFS}}(-\omega)$. Unlike Eq. (8), Eq. (D6) can be nonvanishing for *PT*-symmetric nondegenerate energy bands only leading to the restriction $\chi^{\alpha\beta}_{\mathrm{SFS}}(\omega) = \chi^{\beta\alpha}_{\mathrm{SFS}}(\omega) = \chi^{\alpha\beta}_{\mathrm{SFS}}(-\omega)$. Notice that by replacing the label for the Hamiltonian parametrization $\lambda \to \mathbf{k}$, one reproduces the standard shift nonlinearity as in Refs. [9,12].

Interestingly, although both the KFS contribution in Eq. (C7) and the SFS contribution in Eq. (D6) are intrinsic, their ratio does not appear to carry a particular universal significance. In analogy with the nondegenerate case, the KFS

term tracks the λ derivative of the band energy, whereas the SFS term involves the covariant λ derivative of the interband Berry connection.

APPENDIX E: MBT HAMILTONIAN

In our numerical calculations of nonlinearities of MBT, we adopted low-energy effective Hamiltonian [16,30], with the normal and AFM components of the Hamiltonian in the spin-orbital basis $(|p^+_{z,\mathrm{Bi}},\uparrow\rangle, |p^-_{z,\mathrm{Te}},\downarrow\rangle, |p^-_{z,\mathrm{Te}},\uparrow\rangle, |p^+_{z,\mathrm{Bi}},\downarrow\rangle)^T$. Explicitly, the normal components of the Hamiltonian and the interlayer couplings are

$$h_N(\mathbf{k}) = \epsilon_0(\mathbf{k})\mathbb{I}_4 + \begin{pmatrix} m(\mathbf{k}) & i\alpha k_- & & \\ -i\alpha k_+ & -m(\mathbf{k}) & & \\ & & -m(\mathbf{k}) & i\alpha k_- \\ & & -i\alpha k_+ & m(\mathbf{k}) \end{pmatrix}, \tag{E1}$$

$$t = \begin{pmatrix} t_1 & 0 & -\lambda & 0 \\ 0 & t_2 & 0 & \lambda \\ \lambda & 0 & t_2 & 0 \\ 0 & -\lambda & 0 & t_1 \end{pmatrix}, \tag{E2}$$

with $k_\pm = k_x \pm ik_y$, the dispersive part $\epsilon_0(\mathbf{k}) = \gamma_0 + \gamma k^2$ and massive part $m(\mathbf{k}) = m_0 + \beta_0 k^2$. The set of parameters adopted was extracted from Ref. [16] that was recently used to capture the effective electronic behavior of antiferromagnetic even MBT layers. For the convenience of the reader, the parameters are as follows: $\gamma = 17.0\,\mathrm{eV\,Å^2}$, $m_0 = -0.04\,\mathrm{eV}$, $\beta_0 = 9.40\,\mathrm{eV\,Å^2}$, $\alpha = 3.20\,\mathrm{eV\,Å}$, $m_1 = 0.05\,\mathrm{eV}$, $m_2 = 0.09\,\mathrm{eV}$, $t_1 = -0.0533$ eV, $t_2 = 0.0463\,\mathrm{eV}$, $\lambda = 0.0577\,\mathrm{eV}$.

As we have in our model, the layer Hamiltonian is

$$h_l = h_N(\mathbf{k}) - (-1)^l h_{\mathrm{AFM}}(\mathbf{k}). \tag{E3}$$

APPENDIX F: COMPARISON OF *PT*-ODD OBSERVABLE NONLINEARITIES FOR DIFFERENT τ

Kramers injection response in Eq. (8) is highly sensitive to the scattering time τ. In the main text, we considered $\tau = 0.25$ ps as an illustration. Here, in Fig. 3, we display additional simulation results for $\tau = 1$ ps, 50 fs, 25 fs, 1 fs to cover the range of realistic scattering times [19]. Importantly, for larger scattering times, the Kramers nonlinearities become systematically dominant, showing that they are the leading layer polarization nonlinearities in $MnBi_2Te_4$, which is the same behavior as discussed in the main text.

[1] M. Z. Hasan and C. L. Kane, *Colloquium*: Topological insulators, Rev. Mod. Phys. **82**, 3045 (2010).

[2] J.J. Sakurai and J. Napolitano, *Modern Quantum Mechanics* (Cambridge University Press, Cambridge, 2017).

[3] P. Tang, Q. Zhou, G. Xu, and S.-C. Zhang, Dirac fermions in an antiferromagnetic semimetal, Nat. Phys. **12**, 1100 (2016).

[4] A. Gao, Y.-F. Liu, C. Hu, J.-X. Qiu, C. Tzschaschel, B. Ghosh, S.-C. Ho, D. Bérubé, R. Chen, H. Sun, Z. Zhang, *et al.*, Layer Hall effect in a 2D topological axion antiferromagnet, Nature (London) **595**, 521 (2021).

[5] I. Sodemann and L. Fu, Quantum nonlinear Hall effect induced by Berry curvature dipole in time-reversal invariant materials, Phys. Rev. Lett. **115**, 216806 (2015).

[6] O. Matsyshyn and I. Sodemann, Nonlinear Hall acceleration and the quantum rectification sum rule, Phys. Rev. Lett. **123**, 246602 (2019).

[7] J. E. Sipe and A. I. Shkrebtii, Second-order optical response in semiconductors, Phys. Rev. B **61**, 5337 (2000).

[8] F. de Juan, A. G. Grushin, T. Morimoto, and J. E. Moore, Quantized circular photogalvanic effect in Weyl semimetals, Nat. Commun. **8**, 15995 (2017).

[9] H. Watanabe and Y. Yanase, Chiral photocurrent in parity-violating magnet and enhanced response in topological antiferromagnet, Phys. Rev. X **11**, 011001 (2021).

[10] T. Morimoto and N. Nagaosa, Topological nature of nonlinear optical effects in solids, Sci. Adv. **2**, e1501524 (2016).

[11] J. Ahn, G.-Y. Guo, N. Nagaosa, and A. Vishwanath, Riemannian geometry of resonant optical responses, Nat. Phys. **18**, 290 (2022).

[12] J. Ahn, G.-Y. Guo, and N. Nagaosa, Low-frequency divergence and quantum geometry of the bulk photovoltaic effect in topological semimetals, Phys. Rev. X **10**, 041041 (2020).

[13] N. Wang, D. Kaplan, Z. Zhang, T. Holder, N. Cao, A. Wang, X. Zhou, F. Zhou, Z. Jiang, C. Zhang, S. Ru, H. Cai, K. Watanabe, T. Taniguchi, B. Yan, and W. Gao, Quantum-metric-induced nonlinear transport in a topological antiferromagnet, Nature (London) **621**, 487 (2023).

[14] J.-X. Qiu, C. Tzschaschel, J. Ahn, A. Gao, H. Li, X.-Y. Zhang, B. Ghosh, C. Hu, Y.-X. Wang, Y.-F. Liu, *et al.*, Axion optical induction of antiferromagnetic order, Nat. Mater. **22**, 583 (2023).

[15] J. Godinho, H. Reichlová, D. Kriegner, V. Novák, K. Olejník, Z. Kašpar, Z. Šobáň, P. Wadley, R. P. Campion, R. M. Otxoa, P. E. Roy, J. Železný, T. Jungwirth, and J. Wunderlich, Electrically induced and detected Néel vector reversal in a collinear antiferromagnet, Nat. Commun. **9**, 4686 (2018).

[16] A. Gao, Y.-F. Liu, J.-X. Qiu, B. Ghosh, T. V. Trevisan, Y. Onishi, C. Hu, T. Qian, H.-J. Tien, S.-W. Chen, *et al.*, Quantum metric nonlinear Hall effect in a topological antiferromagnetic heterostructure, Science **381**, 181 (2023).

[17] J. P. Provost and G. Vallee, Riemannian structure on manifolds of quantum states, Commun. Math. Phys. **76**, 289 (1980).

[18] W. J. Jankowski and R.-J. Slager, Quantized integrated shift effect in multigap topological phases, Phys. Rev. Lett. **133**, 186601 (2024).

[19] Q. Ma, R. Krishna Kumar, S.-Y. Xu, F. H. L. Koppens, and J. C. W. Song, Photocurrent as a multiphysics diagnostic of quantum materials, Nat. Rev. Phys. **5**, 170 (2023).

[20] P. Törmä, Essay: Where can quantum geometry lead us? Phys. Rev. Lett. **131**, 240001 (2023).

[21] H. Wang and X. Qian, Ferroicity-driven nonlinear photocurrent switching in time-reversal invariant ferroic materials, Sci. Adv. **5**, eaav9743 (2019).

[22] T. Holder, D. Kaplan, and B. Yan, Consequences of time-reversal-symmetry breaking in the light-matter interaction:

Berry curvature, quantum metric, and diabatic motion, Phys. Rev. Res. **2**, 033100 (2020).

[23] D. Rees, K. Manna, B. Lu, T. Morimoto, H. Borrmann, C. Felser, J. E. Moore, D. H. Torchinsky, and J. Orenstein, Helicity-dependent photocurrents in the chiral Weyl semimetal RhSi, Sci. Adv. **6**, eaba0509 (2020).

[24] O. Matsyshyn, J. C. W. Song, I. S. Villadiego, and L.-K. Shi, Fermi-Dirac staircase occupation of Floquet bands and current rectification inside the optical gap of metals: An exact approach, Phys. Rev. B **107**, 195135 (2023).

[25] F. de Juan, Y. Zhang, T. Morimoto, Y. Sun, J. E. Moore, and A. G. Grushin, Difference frequency generation in topological semimetals, Phys. Rev. Res. **2**, 012017(R) (2020).

[26] L. Gao, Z. Addison, E. J. Mele, and A. M. Rappe, Intrinsic Fermi-surface contribution to the bulk photovoltaic effect, Phys. Rev. Res. **3**, L042032 (2021).

[27] L.-K. Shi, O. Matsyshyn, J. C. W. Song, and I. S. Villadiego, Berry-dipole photovoltaic demon and the thermodynamics of photocurrent generation within the optical gap of metals, Phys. Rev. B **107**, 125151 (2023).

[28] T. G. Rappoport, T. A. Morgado, S. Lannebère, and M. G. Silveirinha, Engineering transistorlike optical gain in two-dimensional materials with Berry curvature dipoles, Phys. Rev. Lett. **130**, 076901 (2023).

[29] O. Matsyshyn, Y. Xiong, A. Arora, and J. C. W. Song, Layer photovoltaic effect in van der Waals heterostructures, Phys. Rev. B **107**, 205306 (2023).

[30] B. Lian, Z. Liu, Y. Zhang, and J. Wang, Flat Chern band from twisted bilayer $MnBi_2Te_4$, Phys. Rev. Lett. **124**, 126402 (2020).

[31] B. A. Bernevig and T. L. Hughes, *Topological Insulators and Topological Superconductors* (Princeton University Press, NJ, 2013).

[32] Y. Gao, Y. Zhang, and D. Xiao, Tunable layer circular photogalvanic effect in twisted bilayers, Phys. Rev. Lett. **124**, 077401 (2020).

[33] L. Z. Tan and A. M. Rappe, Enhancement of the bulk photovoltaic effect in topological insulators, Phys. Rev. Lett. **116**, 237402 (2016).

[34] J. Li, Y. Li, S. Du, Z. Wang, B.-L. Gu, S.-C. Zhang, K. He, W. Duan, and Y. Xu, Intrinsic magnetic topological insulators in van der Waals layered $MnBi_2Te_4$-family materials, Sci. Adv. **5**, eaaw5685 (2019).

[35] L. Šmejkal, J. Sinova, and T. Jungwirth, Emerging research landscape of altermagnetism, Phys. Rev. X **12**, 040501 (2022).

[36] O. Matsyshyn, Data for "Kramers Dichroism in PT Symmetric Magnets" [Data set], Zenodo (2026), https://doi.org/10.5281/zenodo.20732726.